Catalysis Today 171 (2011) 104–115

Contents lists available at ScienceDirect

Catalysis Today

journal homepage: www.elsevier.com/locate/cattod

Effect of the preparation methods and alumina nanoparticles on the catalytic performance of $Rh/Zr_xCe_{1-x}O_2–Al_2O_3$ in methane partial oxidation

Sara Boullosa-Eiras, Tiejun Zhao, De Chen, Anders Holmen*

Department of Chemical Engineering, Norwegian University of Science and Technology Sem Sælands vei 4, N-7491 Trondheim, Norway

ARTICLE INFO

Article history:
Received 25 October 2010
Received in revised form 6 April 2011
Accepted 12 April 2011
Available online 25 May 2011

Keywords:
Methane partial oxidation
Rhodium
Ceria
Zirconia
Alumina

ABSTRACT

Rh supported on $Zr_xCe_{1-x}O_2–Al_2O_3$ ($x = 1, 0.5, 0.25, 0$) catalysts are studied for catalytic partial oxidation of methane to synthesis gas. Alumina based nanocomposites are prepared through a citrate mediated route by modifying the alumina support with cerium and zirconyl nitrates via a simple evaporation-drying or a spray drying method. The effect of the commercial alumina types and the preparation method on the structure and thermostability of the nanocomposites has been studied based on the characterization by XRD, Raman spectroscopy, DTA, TEM and nitrogen adsorption–desorption measurements. Evonik Aeroxide AluC based nanocomposites prepared by spray drying give the highest thermostability concerning the sintering and phase transformation of the composites. Rh with a 0.1 or 0.5 wt.% loading is deposited on these nanocomposites by incipient wetness impregnation method. After calcination at 1173 K for 5 h, these nanocomposites supported Rh catalysts are tested in the fixed-bed reactor for methane partial oxidation. It is found that the smaller c-CeO_2 crystal size in the nanocomposites, i.e. the higher oxygen vacancy concentration, would be responsible of the lower ignition temperature due to the enhanced reducibility, whereas the higher Rh dispersion would be responsible of the higher methane conversion and selectivity to synthesis gas. Additionally the Rh dispersion is found to be linked to the BET surface area. The stability of the nanocomposites is also studied under reaction conditions.

1. Introduction

Catalytic partial oxidation of methane (CPO) is an attractive route for the production of synthesis gas compared to the conventional steam methane reforming process (SMR). It gives a favorable H_2/CO (about 2) ratio of the produced synthesis gas, which is appropriate for processes such as methanol or Fischer–Tropsch synthesis [1]. In addition, CPO can be operated in a millisecond contact-time reactor, being able to provide a compact hydrogen processor for its use in fuel cell electric vehicles [2]. Various transition metals such as Ni [3,4], Co [5], Ru [6], Pt [7], Ir [8] and Rh [9] are found active for this reaction. Among them, Rh based catalysts are presented as the most promising materials due to a better catalytic performance with higher activity, selectivity towards H_2 and CO, and a good stability [10].

The catalytic partial oxidation of methane to synthesis gas is thermodynamically favored at elevated temperatures to obtain a higher conversion and selectivity to H_2 and CO [1]. The mechanism has been frequently studied in the literature [1,4,11–14]. The discussion has mainly focused in the occurrence of the direct or the indirect routes. In the direct route H_2 and CO are the primary reaction products [12,13] whereas in the indirect one CO_2 and H_2O are initially produced by complete oxidation. Afterwards the reforming reaction and water gas shift (WGS) take place to produce syngas [11,14]. However, even though the direct route is theoretically possible, the contribution of the reforming and WGS is typically observed [15–17].

According to the indirect mechanism, the oxygen in the reactant can be rapidly consumed in this period by the deep oxidation of methane, followed by the highly endothermic steam reforming reaction [18]. Although a mild exothermicity appears if the direct conversion of methane to synthesis gas is performed, the deep oxidation of methane is found to be unavoidable in the inlet region of the reactor, even in the short-contact-time reactor [14,18,19]. The high reaction temperature together with the deep oxidation of methane will lead to a very high temperature in the catalyst bodies, especially in the inlet of the reactor, i.e. hot spots. It is well known that the presence of hot spots may also influence the stability of the catalyst and the safety of the process. Controlling the temperature profiles in the reactor is a key issue for the CPO process, which can be reached by effectively removing the produced heat. For this reaction system, metallic foams or monolith supported catalysts are employed to enhance the heat transfer by increasing the heat conductivity of catalyst support. On the other hand, the

* Corresponding author. +4773594151.
E-mail addresses: anders.holmen@chemeng.ntnu.no, holmen@chemeng.ntnu.no (A. Holmen).

0920-5861/$ – see front matter © 2011 Elsevier B.V. All rights reserved.
doi:10.1016/j.cattod.2011.04.021

produced heat by combustion of methane can be consumed by the followed steam reforming reaction. Enhancing the steam reforming reaction rate can substantially reduce the temperature increase, thus making the temperature profile controllable. Wei and Iglesia [20] have pointed out that the rate of steam reforming reaction is linearly correlated with the dispersion of metallic phase. Increasing the Rh dispersion is expected to enhance the steam reforming reaction. However, the preparation of high-temperature stable Rh nanoparticles is challenging due to extreme operating conditions in the CPO. Therefore, developing a catalyst support suitable for stabilizing the Rh nanoparticles is highly interesting. Additionally, lower loading of Rh can significantly reduce the cost of the catalyst.

Although alumina is a very stable material for most oxidation reactions [21], the formation of its thermodynamically stable α-phase is observed when the temperature is increased to 1173 K or higher [21]. Such phase transformations are often accompanied with a gradual decrease in the surface area, simultaneously presenting poor mechanical properties. If the transition alumina is used as a catalyst support for high temperature reactions such as the CPO process, this gradual phase transformation will lead to the possible encapsulation of the metallic phase [22,23]. The poor mechanical properties of α-Al_2O_3 gives a higher cracking possibility as a coating layer in the monolith reactors, especially in the temperature changes such as the ignition and extinction periods [24]. Directly using α-Al_2O_3 may avoid the loss of the active phase and reduce the risk for cracking. However, the stabilization of metal nanoparticles on α-Al_2O_3 is difficult owing to its low surface area and inert surface. Therefore, developing a catalyst support aiming at obtaining high dispersed Rh nanoparticles on it in a high temperature system such as the CPO process is highly interesting.

Attempts to increase the stability of the transition alumina have been reported during the last decade [25–28]. It has been proved that the introduction of an extra phase into the parent material enhances the stability of the support [29–31]. $Zr_xCe_{1-x}O_2$–Al_2O_3 nanocomposites have been studied mainly focusing in its application towards the so-called Three Way Catalysts (TWC) [25,32–34]. Afterwards, the research has been also expanded to reactions such as methane partial oxidation [27,35,36], CO_2 reforming [37], ethanol steam reforming [38,39] or other systems [40–44]. The influence of several variables on the properties of the final product has been investigated for this system. Researchers have focused on the nature of the cerium, zirconium precursor [45], the preparation method [27,28,46,47], the Ce/Zr ratio [36], the mixed oxide–alumina ratio [23,48] or the thermal treatment effect [49]. However, to our knowledge, the nature of the alumina itself has not been yet considered. γ-Al_2O_3 can be prepared from different precursors such as $Al(NO_3)_3$ $9H_2O$ [48,50] and $Al(OC_4H_9)_3$ [29], or provided by different producers [42,44,51]. The physico-chemical properties of these Al_2O_3 powders are strongly dependent on the preparation method and the subsequent treatments. Therefore, a suitable method to combining the alumina type and doped oxide precursors are also highly crucial.

In this article, we report the influence of two commercial alumina samples and two preparation methods on the structure and thermal stability of 5 wt.% $Zr_xCe_{1-x}O_2$–Al_2O_3 nanocomposites. The evolution of the physico-chemical properties of these nanocomposites during high temperature treatments in static air is systematically studied based on the various characterization techniques. The produced composites are used as catalyst support to deposit the Rh metallic phase by impregnation. The catalytic performance of these Rh supported on $Zr_xCe_{1-x}O_2$–Al_2O_3 nanocomposites for the CPO process is evaluated in a quartz fixed-bed. The ignition and extinction behavior and the stability of these catalysts for CPO are as well studied.

2. Experimental

2.1. Catalyst preparation

Two different alumina samples are used in this contribution: Evonik Aeroxide AluC and Sasol Puralox SCCa are denoted as AluC and Puralox, respectively. AluC is an alumina powder produced by flame hydrolysis [52]. It has a crystalline structure consisting of the metastable γ- and δ-forms instead of the stable α-form. The primary particle size is in the range of 13 nm and a specific surface area around 100 m^2/g. At temperatures above 1473 K, it can be transformed to α-form [52]. Puralox is a widely employed material in the catalyst industry. The specific surface area for uncalcined Puralox powders is around 170 m^2/g with a crystalline structure of γ-phase.

$Zr_xCe_{1-x}O_2$ (5 wt.%)–Al_2O_3 nanocomposites are prepared as follows. It should be noticed that $Zr_xCe_{1-x}O_2$ is used to express the chemical composition, not for a solid solution. A certain amount of zirconyl nitrate ($ZrO(NO_3)_3$ xH_2O, 37.5 wt.% ZrO_2) cerium nitrate ($Ce(NO_3)_3$ $6H_2O$) and citric acid ($C_6H_8O_7$) are dissolved into deionized water followed by adding polyethylene glycol (0.1 g/mL_{H_2O}) to form a complex solution. Then, the weighed alumina powder is gradually added into the above complex solution under vigorous stirring to produce a suspension. A detailed study on the preparation method has been reported elsewhere [53]. Two drying procedures have been followed for obtaining the nanocomposites:

2.1.1. Evaporation-drying method

The water in the former suspension is evaporated at 358 K for 2 days to form a dried solid. Both AluC and Puralox have been used for the preparation of such nanocomposites. AluC powders prepared employing this procedure are identified as AluCev.

2.1.2. Spray drying

Using a Lab-Plant SD-06 Laboratory Scale Spray Dryer, the suspension is entrained into a chamber by the heated gases through a nozzle. The obtained powders are collected in a bottle. The pump rate is 120 mL/h, the inlet temperature 438 K and the air flow 4.3 m/s. Only AluC-based materials are prepared by this method due to the large size of the Puralox powder. The materials prepared in this way will be identified like AluCsp.

The final powdered composites are produced after these dried solids are treated in air at different temperatures (from 1173 to 1473 K) for 5 h. For the sake of comparison, $Zr_xCe_{1-x}O_2$ is also prepared by a similar procedure without including the Al_2O_3 powder. For the preparation of the Rh catalysts, rhodium nitrate is deposited on the calcined $Zr_xCe_{1-x}O_2$–Al_2O_3 support by the incipient wetness impregnation at room temperature. The prepared catalyst is kept at room temperature overnight. Subsequently, the formed solid is calcined at 1173 K for 5 h.

2.2. Catalyst characterization

2.2.1. X-ray diffraction (XRD)

X-ray diffraction (XRD) patterns of these composites are recorded at room temperature on a Bruker AXS D8 Focus diffractometer using CuKα radiation (λ = 1.54 Å). The X-ray tube voltage is set to 40 kV and the current to 50 mA. XRD patterns are collected in the range of 2θ from 20° to 85° for nanocomposites, (0.01°/step, integration time of 1 s/step) and 2θ from 27° to 32° for $Zr_xCe_{1-x}O_2$ phase (0.02°/step, integration time of 10 s/step). Diffractograms are analyzed by employing the Topas program applying the Rietveld fitting [54] to estimate the alumina phase composition and applying the Pawley method [55] to calculate the crystal size of $Zr_xCe_{1-x}O_2$ and Al_2O_3 in these composites.

2.2.2. Differential thermal analysis (DTA)

DTA is carried out using a Netzsch Jupiter STA 449C in oxidizing atmosphere to investigate the phase transition of the different supports. The samples are heated to 1803 K at a heating rate of 10 K/min in air. The total flow, 80 mL/min air and 20 mL/min argon (protective gas for weighing house), is fed through the sample compartment.

2.2.3. Textual properties

Nitrogen adsorption–desorption isotherms of the samples are measured with a Micromeritics TriStar 3000 instrument, and the data are collected at liquid nitrogen temperature, 77 K. Prior to the measurements, the samples are outgassed at 473 K overnight. The surface area is calculated from the Brunauer–Emmett–Teller (BET) equation. The Barrett–Joyner–Halenda model is chosen for calculation of pore sizes.

2.2.4. Raman spectroscopy

Raman spectra are collected on a Horiba Jobin Yvon LabRAM HR800 spectrometer. The emission lines at 633 nm from a He–Ne laser are focused on the sample with a 100× objective.

2.2.5. Electron microscopy

The morphology of the solid is examined by the HRTEM (JOEL JEM 2010). The powdered samples are suspended in absolute ethanol for 2 min with ultrasonication, and a droplet of this suspension is dipped onto the holey carbon-coated copper grid.

2.2.6. H_2 chemisorption

The Rh dispersion measurements of the calcined catalysts are performed by volumetric hydrogen chemisorption on a Micromeritics ASAP 2010C instrument. The calcined catalyst (100 mg) is loaded in a U-shaped quartz reactor, where it is initially evacuated at 303 K for 1 h. Afterwards it is reduced in flowing H_2 at 923 K for 60 min (heating rate 10 K/min). After reduction, the samples are evacuated at 673 K for 240 min, then cooled down to 303 K, and evacuated for another 30 min. The adsorption isotherm measurements are carried out at 303 K and 191 K based on the adsorbed amount of hydrogen at different pressures in the range 2–200 mmHg. Adsorbed volumes are determined by extrapolation to zero pressure of the linear part of the adsorption isotherm on the interval 2–100 mmHg. A chemisorption stoichiometry of H:Rh = 1:1 is assumed. With the objective of avoiding the possible H_2 spillover on the Ce containing catalysts, volumetric hydrogen chemisorption is performed at 191 K [56,57].

2.3. Catalytic activity

Catalytic partial oxidation of methane is carried out in a quartz reactor (10 mm i.d.) at atmospheric pressure. A movable thermocouple is placed in a quartz tube inserted into the quartz reactor, enabling the measurement of the apparent gas temperature profile. Methane and air with desired flow rates are mixed and fed into the reaction system. A condenser is set to remove the produced water. Another thermocouple is set on the outer wall of the reactor outlet to control the furnace temperature. Typically, 10 mg of pelletized catalyst (sieve fraction 100–200 μm) diluted with α-alumina are used in each measurement. The employed gas hourly space velocities (GHSV) are 1500 L_{CH4}/g_{cat} h. The reaction temperature interval is in the range of 673–1173 K. A reactant mixture of methane and air is used with a ratio CH_4:O_2:N_2 of 2:1:3.72. The product analysis is carried out by a gas chromatographer (GC) (Agilent 6980) coupled with a thermal conductivity detector (TCD) and a flame ionization detector (FID). The H_2 and H_2O concentrations are determined through the hydrogen and oxygen balance respectively.

The ignition–extinction behavior over different catalysts is studied by increasing gradually the furnace temperature from 573 K to 1173 K at a heating rate of 10 K/min. Subsequently, the reactor is cooled down until the reaction becomes autothermal.

The stability of the catalyst is studied by increasing the furnace temperature to 1173 K with a heating rate of 10 K/min. The catalyst is maintained on reaction conditions during 48 h while product analysis is performed each 23 min.

Results are presented as function of the outlet temperature, which is defined as the temperature at the outlet of the catalytic bed measured with the internal movable thermocouple.

3. Results and discussion

3.1. Structural properties of the nanocomposites

The nanocomposite samples, $Zr_xCe_{1-x}O_2$–Al_2O_3, are studied employing XRD, N_2 adsoption–desorption measurements, TEM, Raman spectroscopy and DTA measurements. The results regarding the Puralox sample have been reported elsewhere [58,59]. Here, a comparison of the results obtained for both aluminas, Puralox and AluC, and preparation methods is presented.

3.1.1. Alumina phase characterization in the nanocomposites

The two alumina powders, AluC and Puralox, calcined at temperatures between 1173 and 1473 K are investigated here. XRD patterns are measured for these powders at room temperature. Both AluC and Puralox treated at 1173 K and 1273 K for 5 h present almost identical diffractograms, dominating the δ-Al_2O_3 together with some θ-phase. The phase composition for the alumina powders treated at 1373, 1423 and 1473 K has been estimated based on the XRD profiles. Those materials are additionally investigated employing Raman spectroscopy. In previous studies [58] we have demonstrated that visible Raman spectroscopy excited by 633 nm is a useful tool for investigating the alumina phase transformations in the Raman shift interval between 1000 and 2000 cm^{-1}. The comparison of these results with the ones from XRD gives further details in the occurrence of the alumina phase transitions. In such study we have identified the peaks at Raman shift ca. 1176 and 1260 cm^{-1} as related with the θ-phase, whereas the peaks at 1370 and 1397 cm^{-1} were attributed to the α-Al_2O_3. Based on the integration of the peaks related to each of the alumina phases (α- and θ-), the calculation of the alumina phase composition is performed for each of the powders. The obtained results are in agreement with those estimated by XRD employing the Topas program. The alumina phase composition for AluC and Puralox is presented in Fig. 1a. It is observed that, for the AluC sample (3) almost no α-Al_2O_3 is observed and θ-Al_2O_3 is dominant in the solid even after aging at 1473 K during 5 h. In contrast, only the thermodynamically stable α-Al_2O_3 can be observed after heating treatments at 1373 K for the Puralox sample (1) in Fig. 1a.

3.1.1.1. Effect of the water treatment on the raw materials. It is known that water vapour accelerates the crystallization and structural change in oxide supports [21]. The evaporation-drying procedure for preparing the $Zr_xCe_{1-x}O_2$–Al_2O_3 composites involves the 48 h treatment in water solution. Therefore, the effect of the water treatment on the physico-chemical properties of AluC and Puralox is studied here. The resulting powders are also calcined at temperatures between 1173 and 1473 K for 5 h. The alumina phase composition for such water treated materials is estimated based in XRD diffractograms and summarized in Fig. 1a, sample (2) corresponds to the water treated Puralox powders, and sample (4) to the water treated AluC powders. Correspondingly, untreated aluminas (1 and 3) are also shown in Fig. 1a. It is observed that for the AluC samples (3 and 4), the water treatment will accelerate

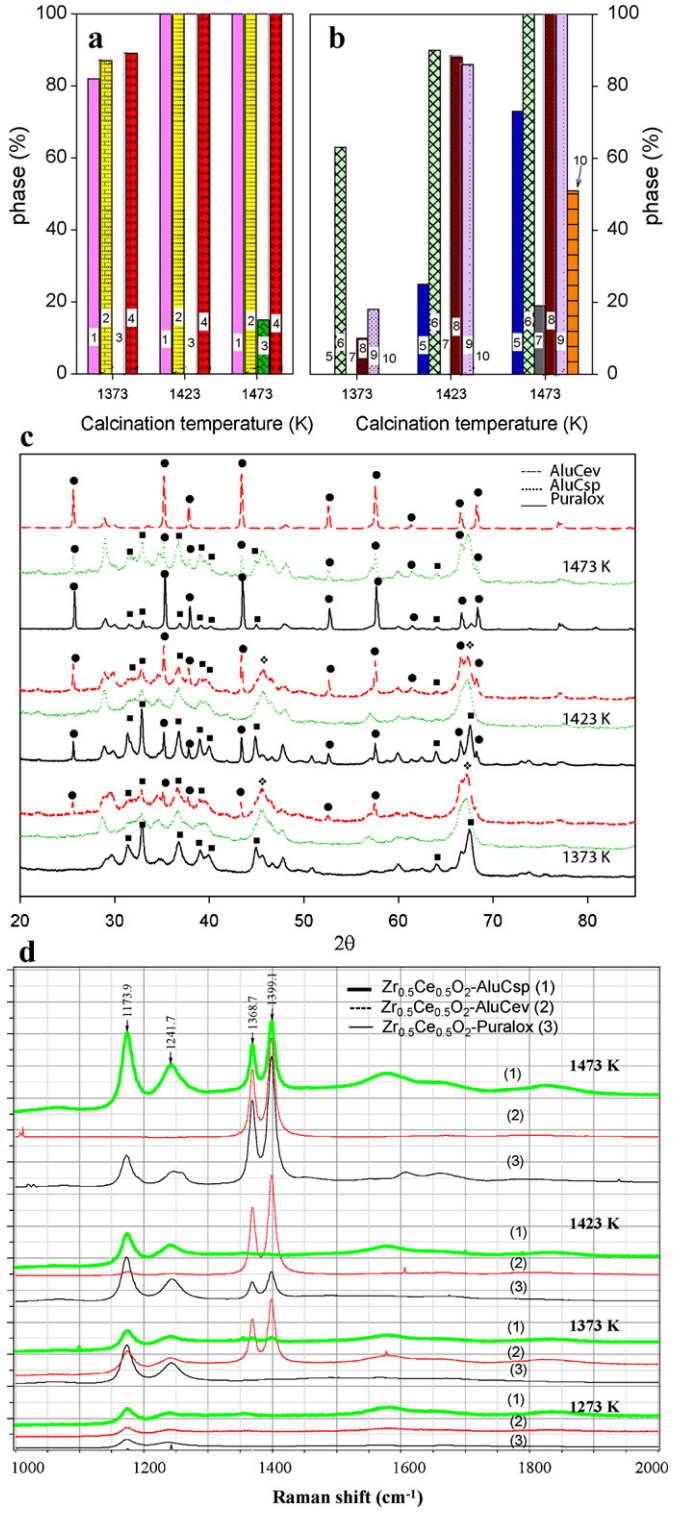

Fig. 1. (a) Summary of the alumina phases composition for 1-Puralox, 2-Puralox water treated, 3-AluC, 4-AluC water treated, (b) summary of the alumina phases composition for the nanocomposites: 5-$Zr_{0.5}Ce_{0.5}O_2$–Puralox, 6-$Zr_{0.5}Ce_{0.5}O_2$–AluCev, 7-$Zr_{0.5}Ce_{0.5}O_2$–AluCsp, 8-CeO_2–Puralox, 9-CeO_2–AluCev, 10-CeO_2–AluCsp samples treated at 1373, 1423 and 1473 K during 5 h. The phase composition is calculated in bases of XRD for the aluminas and Raman for the nanocomposites, (c) X-ray diffraction patterns of $Zr_{0.5}Ce_{0.5}O_2$–Puralox compared with $Zr_{0.5}Ce_{0.5}O_2$–AluCev (▬ ▬ ▬) and $Zr_{0.5}Ce_{0.5}O_2$–AluCsp (• • • • • •). Samples aged for 5 h at temperatures between 1373 and 1473 K. Data collected at 0.02°/step between $2\theta = 20°$ and 85° (●, α-Al_2O_3; , θ-Al_2O_3; ❖, δ-Al_2O_3), and (d) visible Raman spectra of $Zr_{0.5}Ce_{0.5}O_2$–AluCsp (1) compared with $Zr_{0.5}Ce_{0.5}O_2$–AluCev (2) and $Zr_{0.5}Ce_{0.5}O_2$–Puralox (3). Samples are calcined at temperatures between 1273 and 1473 K for 5 h. Spectrum recorded at 633 nm in the Raman shift interval between 1000 and 2000 cm^{-1}.

the phase transformation to α-Al_2O_3. For the selected calcination temperatures, the α-phase contribution is almost the same for the two Puralox samples (1 and 2). Nanosized AluC (average 13 nm) prepared from flame hydrolysis is not stable in the water probably due to its high surface energy, which can strongly bonded with water, thus promoting the sintering during the calcination process.

3.1.1.2. Effect of calcination temperature on alumina phase in the nanocomposites. Nanocomposites with a 5 wt.% loading of $Zr_xCe_{1-x}O_2$–AluC have been prepared through spray drying or evaporation-drying method. The samples are subjected to heat treatments in the interval 1173–1473 K for 5 h. The recorded XRD-patterns are similar regardless of the alumina and method employed for heating treatments below 1373 K. Therefore, only XRD patterns for samples calcined at temperatures between 1373 and 1473 K are shown in Fig. 1c. The figure is presenting the results for AluC nanocomposites prepared by evaporation-drying and spray drying method, denoted as AluCev and AluCsp, respectively. For comparison, $Zr_{0.5}Ce_{0.5}O_2$–Puralox (solid black line) is also shown in this figure. For the samples calcined at 1373 K, α-Al_2O_3 phase only appear in the AluCev based composite. When the nanocomposites are treated at temperatures over 1423 K, α-Al_2O_3 can be found on the AluCev and Puralox based composites, whereas no obvious α-Al_2O_3 is identified in the AluCsp sample. At 1473 K, α-Al_2O_3 is found in these three samples. However, a relatively lower peak intensity of α-Al_2O_3 phase can be observed in the AluCsp nanocomposite compared with AluCev and Puralox ones. From these observations, it seems that the AluCsp sample owes the highest thermal stability in these three composites.

Fig. 1d presents a comparison of the visible Raman spectra for the $Zr_{0.5}Ce_{0.5}O_2$–Al_2O_3 nanocomposites using Puralox (thin solid line) and AluC by evaporation drying (dotted line) and spray drying method (thick solid line). Samples are calcined at temperatures between 1173 and 1473 K for 5 h. It is noticed that the three materials after treated at 1273 K for 5 h present a similar spectrum. However when the calcination temperature is raised to 1373 K the peaks identified with α-Al_2O_3 (peaks at ca. 1370 and 1397 cm^{-1}) are already found in the AluCev sample. These specific peaks ascribed to the α-Al_2O_3 phase start to appear for the Puralox based composites when the samples are calcined at 1423 K for 5 h, whereas no such peaks appear on the AluCsp based sample. When the calcination temperature is raised to 1473 K, the specific α-Al_2O_3 peaks appear in all these three samples. However, in the AluCev sample, no peaks for θ-phase (bands at ca. 1176 and 1260 cm^{-1}) are identified, implying that the Al_2O_3 phase in this sample is completely transformed into α-phase. In the AluCsp and Puralox sample, the peaks for θ-phase and α-phase co-exist. However, much higher peak intensity for θ-Al_2O_3 can be observed on the AluCsp sample. Raman results in Fig. 1d are in well agreement with those reported from XRD in Fig. 1c.

The alumina phase composition has been calculated on bases of visible Raman spectra and XRD diffractograms. The results have been compared and they are displayed in Fig. 1b. As previously reported for the Puralox nanocomposites in an earlier study, visible Raman is more sensitive to the α-phase at the lower calcination temperature (1373 K) [59]. The results derived from the Raman study are selected in this case due to the lack of interference by the Ce–Zr phase. The alumina phase composition for these samples is summarized in Fig. 1b. 100%, 88% and 19% of α-Al_2O_3 are observed for $Zr_{0.5}Ce_{0.5}O_2$–AluCev (6), $Zr_{0.5}Ce_{0.5}O_2$–Puralox (5) and $Zr_{0.5}Ce_{0.5}O_2$–AluCsp (7), respectively, when the materials are treated in air at 1473 K for 5 h. These results reveal that the preparation method has a significant effect on the catalyst properties suggesting that the spray drying method provides a more uniform oxide layer on the alumina than the evaporation method.

The results for the CeO_2–Al_2O_3 (8, 9 and 10) are also displayed in Fig. 1b. It is confirmed the important contribution of the α-phase for the AluCev (9) samples even after treatment at 1373 K. Additionally, the α-phase is not presented in any of the materials prepared with the spray dryer until calcination at 1473 K for 5 h. Besides, for the case of the $Zr_{0.5}Ce_{0.5}O_2$–AluCsp sample θ-Al_2O_3 is dominant in the solid for such heating treatment.

Based on the above observations, it is possible to conclude that when the materials are prepared with the evaporation-drying method for both Puralox and AluCev supports, higher temperatures are needed for the Puralox-based samples to form the α-Al_2O_3 phase compared with the AluCev ones. Besides, the detrimental effect of water in the slow evaporation method is confirmed by Raman and XRD when the results of AluCev and AluCsp are compared.

3.1.1.3. Effect of calcination time on the alumina phase in the nanocomposites. The effect of the calcination time on the α-alumina formation has been studied by calcining the $Zr_xCe_{1-x}O_2$–Al_2O_3 (x = 0.5, 0) at 1373 K for 24 h. Those materials are investigated employing XRD. After calcination for 24 h the water treated parent materials (AluC and Puralox) show a complete transformation to the α-alumina phase corresponding to a typical α-alumina pattern of sharp and strong peaks (for simplicity and similarity to the data shown in Fig. 1c, the diffractograms after calcination during 24 h are not shown here).

The comparison of the alumina phase composition for the composite materials calcined at 1373 K for 5 and 24 h can give an insight into the thermal stability of the material since the thermal stability of the composites can be reflected by the delay in the α-alumina formation. A clear difference in the α-phase contribution is observed for the sample CeO_2–Al_2O_3. Significantly higher peak intensity for α-Al_2O_3 in XRD patterns are found on the AluC composites synthesized by evaporation-drying compared to the one prepared by spray drying The contribution of the alumina phases is estimated by using Topas software for these three CeO_2–Al_2O_3 materials. For AluCev-based composite, 85% of the alumina present is α-phase under such calcination conditions. In contrast, a fraction of α-alumina of approximately the 8% is found for the Puralox-ev based sample and no α-phase is detected when the spray drying method is employed (AluCsp sample). Regarding the sample $Zr_{0.5}Ce_{0.5}O_2$–Al_2O_3, the α-phase is not observed in the case of the Puralox sample or the AluCsp, whereas 20% of the alumina contented in the $Zr_{0.5}Ce_{0.5}O_2$–AluCev is under the α-phase.

These results show a better thermostability of the Puralox-based samples as indicated by delaying the α-alumina formation than the AluC-based samples when the evaporation-drying method is used. This is probably related to the better stability of parent Al_2O_3 during the water treatment. For the AluC sample, a fast spray drying procedure can suppress the alumina sintering to a large extent, thus showing the best thermal stability.

3.1.2. Effect of the calcination temperature on the $Zr_xCe_{1-x}O_2$ phase in the nanocomposites

Diffractograms with lower scanning speed are recorded in the range 27–32° for studying the $Zr_xCe_{1-x}O_2$ phase in the nanocomposites. The addition of ceria, zirconia or mixed oxides of both, lead to the appearance of new diffraction peaks. The peak related with cubic ceria (c-CeO_2) which presents the higher intensity is placed at 2θ = 28.54° whereas the one attributed to the tetragonal zirconia (t-ZrO_2) is located at 2θ = 30.2°. For those materials that contain ceria–zirconia mixtures the peak is shifted from 28.54° to higher 2θ values as a function of the zirconium oxide content. According to the literature [46,49] such shift is an indication that the Zr is introduced into the cerium lattice. Fig. 2a displays a comparison of the results for the $Zr_{0.5}Ce_{0.5}O_2$–Al_2O_3 nanocomposite synthesized

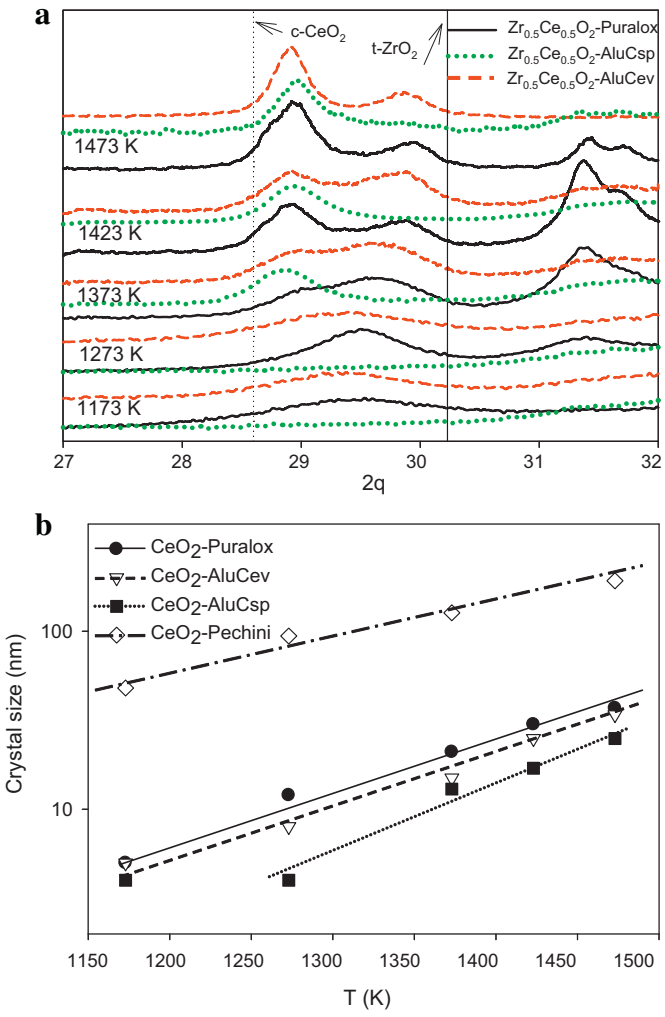

Fig. 2. (a) X-ray diffraction patterns of $Zr_{0.5}Ce_{0.5}O_2$–Puralox (—) compared with $Zr_{0.5}Ce_{0.5}O_2$–AluC (▬ ▬ ▬) and $Zr_{0.5}Ce_{0.5}O_2$–AluCsp (• • • • • •). The samples are aged for 5 h at temperatures between 1173 and 1473 K. The vertical dotted line marks the characteristic position of cubic ceria (2θ = 28.54°) whereas the solid line shows the position of tetragonal zirconia (2θ = 30.2°). Data collected at 0.02°/step with integration times of 10 s/step between 2θ = 27° and 32° and (b) c-CeO_2 crystal size evolution for CeO_2–Al_2O_3 nanocomposites aged for 5 h with calcination temperatures between 1173 and 1473 K (●, CeO_2–Puralox; ▽ CeO_2–AluCev; , CeO_2–AluCsp; , CeO_2-Pechini). Data based on XRD results collected at 0.02°/step between 2θ = 20° and 85°.

with the two alumina samples prepared by the two methods in the interval of 2θ between 27° and 32°. Puralox is shown as a solid line, AluCev as a dashed line, and AluCsp as a dotted line.

Kozlov et al. [46] proposed a simple method for the determination of the composition of the Zr–Ce phases based on the JCPDS (Joint Committee on Powder Diffraction Standards). The results for $Zr_{0.5}Ce_{0.5}O_2$–Al_2O_3 nanocomposites in Fig. 2a show that the supports treated at temperatures lower than 1373 K present a single diffraction peak at around 2θ = 29.5° for the Puralox sample and 29.4° for the AluCev one. The 2θ value is slightly higher than theoretical value for the $Zr_{0.5}Ce_{0.5}O_2$ composition suggesting the formation of a mixed oxide richer in zirconia. The reason for this behavior could be due to an additional cerium oxide rich phase not observable under XRD due to its lower cerium oxide loading. At calcination temperatures higher than 1423 K, for the Puralox and AluCev samples, the single peak is splitting in two as predicted by the phase diagram for the system CeO_2–ZrO_2 [60]. The thermodynamically stable t-ZrO_2 rich and c-CeO_2 rich phases are formed. On the other hand, for the AluCsp sample, it is not possible

to detect any peak related with the Zr–Ce phases until calcination at 1373 K where a single peak at ca. 28.9° appears. This peak corresponds to an oxide richer in ceria than expected, implying that a highly dispersed zirconia phase might be present on the surface of the alumina. The crystal size evolution with the temperature for the Zr–Ce phases has been estimated employing Topas software. The larger crystal size value has been selected when two phases are observed in the diffractogram. The low intensity of the peak related to the Zr–Ce phase at calcination temperatures lower than 1373 K indicates a highly dispersed phase on the alumina surface with a small crystal size. The increased calcination temperatures lead to the formation of better defined peaks proving the higher crystallinity of the sample. The calculation of the crystal sizes performed at a calcination temperature of 1473 K for the $Zr_{0.5}Ce_{0.5}O_2$–Al_2O_3 samples have shown the following trend: $Zr_{0.5}Ce_{0.5}O_2$–AluCev (24 nm) > $Zr_{0.5}Ce_{0.5}O_2$–Puralox (14 nm) > $Zr_{0.5}Ce_{0.5}O_2$–AluCsp (11 nm) proving the higher dispersion of the Zr–Ce oxide on the alumina phase for the sample prepared with the spray drying. A high surface area resulted in the delayed formation of the α-alumina phase in the spray-drying prepared sample would be a plausible explanation for this behavior. Therefore, the smaller crystal size of the alumina in the AluCsp sample would provide a higher barrier for sintering in this material than in the other two.

Fig. 2b reports the evolution of the c-CeO_2 crystal size with the calcination temperature for the CeO_2–Al_2O_3 nanocomposites. The crystal size has been calculated employing the Topas software based on the XRD results. It is observed that those samples prepared with AluC retain a smaller crystal size than the Puralox ones for each of the selected calcination temperatures. It is believed that the AluC powders are helpful for dispersing better the c-CeO_2 due to its smaller primary size, when compared with the Puralox ones. From the comparison of both samples prepared with AluC by the two different methods, evaporation and spray drying, it is found that the c-CeO_2 crystal size remains always smaller for the material prepared by spray drying. We reckon that the slow water treatment leads to the agglomeration of the AluC nanopowders, and in addition, the α-phase formation at lower temperature for the CeO_2–AluCev contributes to the c-CeO_2 sintering. c-CeO_2 powders have been prepared without using alumina by the so-called Pechini method. In this case much bigger crystals are found as shown in Fig. 2b. The c-CeO_2 crystal size evolution with the aging time has also been followed for the sample treated at 1373 K for 5 and 24 h. As expected, the c-CeO_2 crystal size increased with the calcination time but the samples CeO_2–AluCsp and CeO_2–Puralox show a better stability against sintering. The calculated crystal size for the ceria in CeO_2–AluCsp after aging calcination for 5 h at 1373 K is

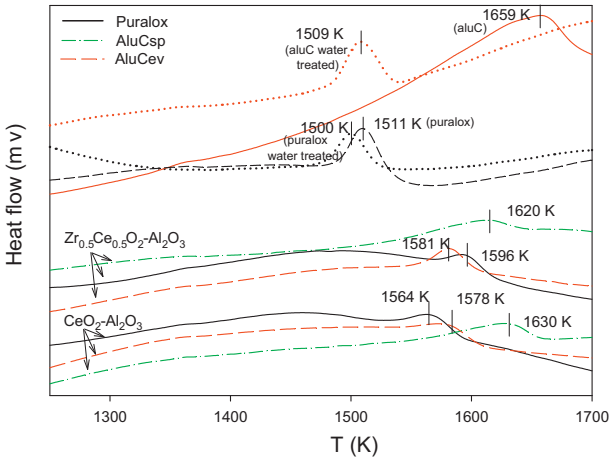

Fig. 3. DTA profiles for $Zr_xCe_{1-x}O_2$–Puralox (——) compared with for $Zr_xCe_{1-x}O_2$–AluCev (▬▬▬) and $Zr_xCe_{1-x}O_2$–AluCsp (▬·▬·▬) measured in the temperature interval 1250 K and 1700 K compared with AluC (▬▬), Puralox (·····), AluC water treated (• • • •) and Puralox water treated (—-) (heating rate: 10 K/min; air flow = 80 mL/min).

12 nm whereas it is 15 nm for the 24 h case. For the Puralox sample treated for 5 h the crystal size is 22 nm and 30 nm when the calcination time is increased to 24 h. Finally the sample AluCev presents a c-CeO_2 crystal size of 15 nm after heating treatment for 5 h, and this value is increased to 26 nm when the aging calcination time is raised to 24 h. It is believed that the nature of the alumina and the preparation method play an important role in the sintering of the c-CeO_2 nanoparticles.

3.1.3. DTA results of the nanocomposites

Fig. 3 shows the DTA curves for the nanocomposites synthesized employing AluC and Puralox in the temperature interval from 1273 K to 1700 K. At temperatures lower than 1273 K, similar profiles are observed for all the materials. The exothermic peak observed in the interval 1500–1660 K corresponds to the transformation to α-Al_2O_3. The DTA profiles for AluC, Puralox and the samples after the water treatment are also presented in Fig. 3. It is observed that in the case of AluC the water treatment has a pronounced effect on the α-Al_2O_3 formation. For the AluC itself, the exothermic peak is observed at 1659 K, whereas for the water treated material, this peak appears at 1509 K. In the Puralox case, a small difference of temperature is found for the transformation peak as indicated in Fig. 3. These results are in agreement with those reported in Fig. 1a where the alumina phase composition estimated

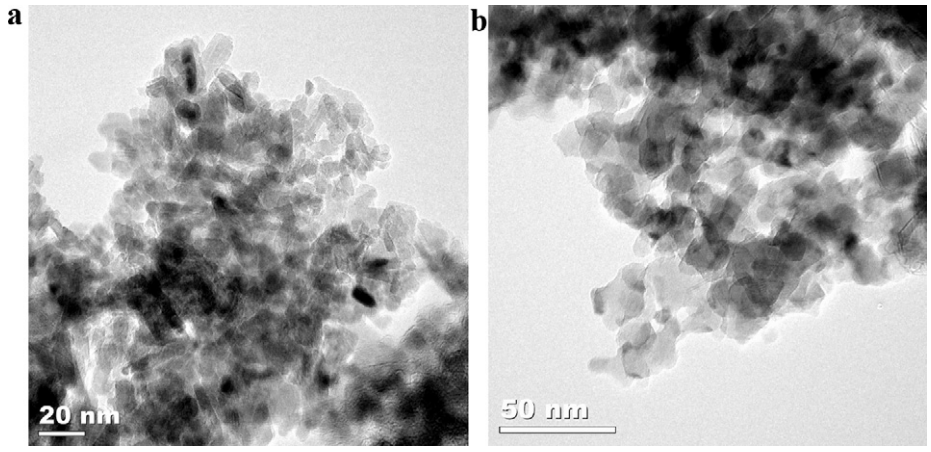

Fig. 4. TEM micrograph of (a) CeO_2–Puralox and (b) CeO_2–AluCev.

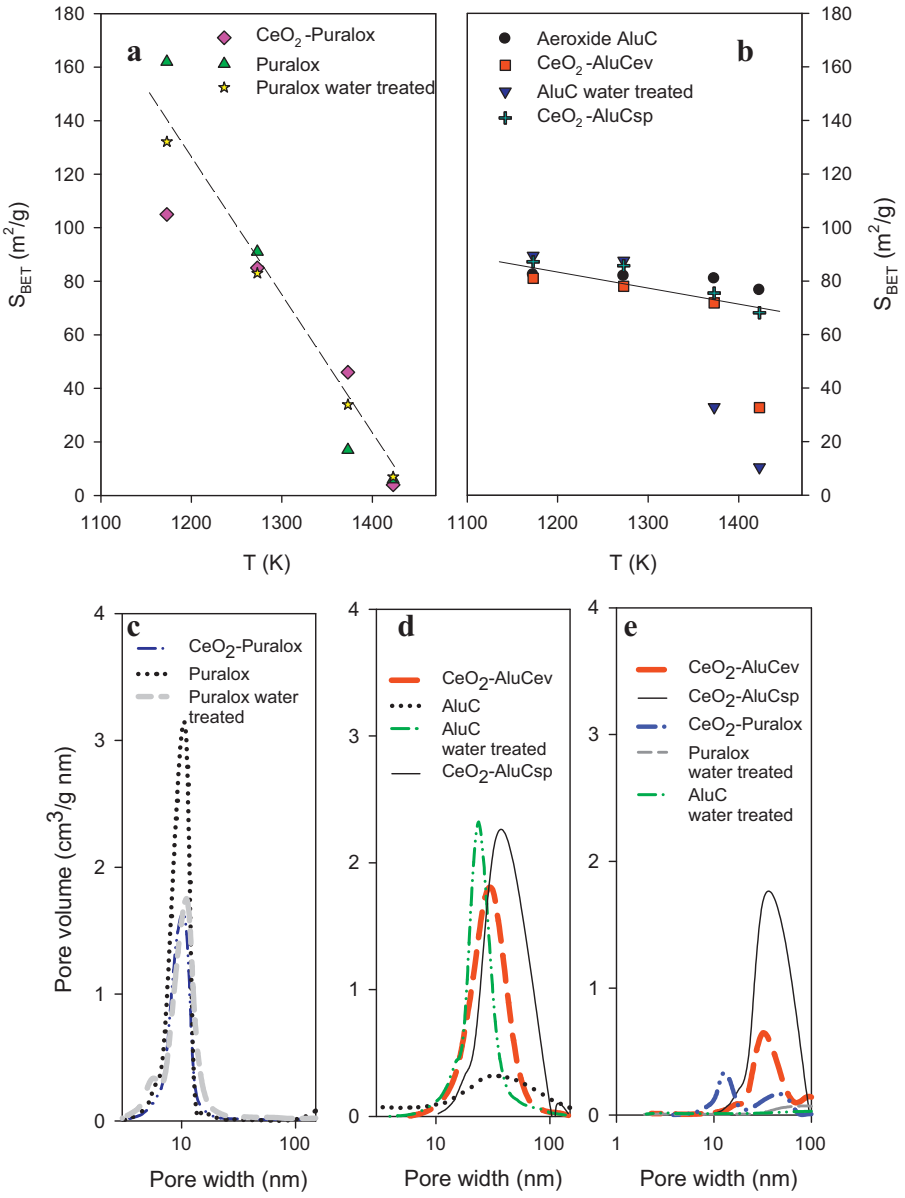

Fig. 5. (a) BET surface area evolution with the calcination temperature for $Zr_{0.5}Ce_{0.5}CeO_2$–Puralox nanocomposites compared with the raw materials (▲, Puralox; ★, Puralox water treated; ◆, $Zr_{0.5}Ce_{0.5}O_2$–Puralox; ○, $Zr_{0.5}Ce_{0.5}O_2$), (b) BET surface area evolution with the calcination temperature for $Zr_{0.5}Ce_{0.5}O_2$–AluC nanocomposites compared with the raw materials (●, Aeroxide AluC; ▼, AluC water treated; ■, $Zr_{0.5}Ce_{0.5}O_2$–AluCev; ✚, $Zr_{0.5}Ce_{0.5}O_2$–AluCsp; ○, $Zr_{0.5}Ce_{0.5}O_2$), (c–e) effect of the introduction of CeO_2 in the pore size distribution for (c) Puralox after calcination at 1173 K during 5 h, (d) AluC samples after calcination at 1173 K during 5 h and (e) Puralox and AluC samples after calcination at 1423 K during 5 h.

based on XRD and Raman profiles at calcination temperatures over 1373 K are listed. It has been shown that the water treatment of the alumina will promote the formation of α-phase, especially for AluC.

Furthermore, a clear delay of the exothermic peak is found in the $Zr_xCe_{1-x}O_2$–Al_2O_3 if we compare the water treated Al_2O_3 as the base. The difference in temperature is in the range of 60–110 K. It is found that the AluC based nanocomposites prepared by spray drying show a higher transformation temperature for α-Al_2O_3 formation compared with the samples prepared by evaporation-drying method. This observation agrees well with the XRD and Raman results as shown in the previous section. Changes of the $Zr_xCe_{1-x}O_2$ composition will not influence the transformation temperature to α-Al_2O_3 concerning the $Zr_{0.5}Ce_{0.5}O_2$–Al_2O_3 and CeO_2–Al_2O_3 samples. It is noticed that the fresh AluC presents the highest thermal stability in the DTA trace, which is in agreement with the XRD patterns.

3.1.4. Morphology of the samples

The morphology of the for $Zr_{0.5}Ce_{0.5}O_2$–Al_2O_3 nanocomposites after heat treatment at 1173 K for 5 h is examined with TEM and presented in Fig. 4a and b, where Fig. 4a is showing the global morphology for the Puralox sample, and Fig. 4b for the AluC nanocomposites. The different morphology of both kind of materials is clearly observed, where the Puralox-based ones are presenting a nanorod-like shape whereas spherical nanosized particles are observed in the case of the of the AluC sample in Fig. 4b.

3.2. Textural properties of the nanocomposites

BET surface area measurements are performed for the alumina powders treated at 1173, 1273, 1373 and 1423 K for 5 h. The S_{BET} evolution is shown in Fig. 5a and b for the Puralox and AluC-based materials, respectively. It is found that Puralox is more sensitive to the calcination temperature than AluC. It is observed

Table 1
Rh dispersion (%) and particle size (nm) values calculated in bases of H_2 chemisorption results. Irreversible H_2 adsorption at 303 K and 195 K calculated assuming Langmurian adsorption.

	Rh loading 0.1 wt.%		Rh loading 0.5 wt.%	
	Dispersion (%)	Particle size (nm)	Dispersion (%)	Particle size (nm)
Puralox[a]	29	3.8	26	4.2
AluC[a]	29	3.8	20	5.4
$Zr_{0.5}Ce_{0.5}O_2$–Puralox[b]	41	2.7	30	3.7
$Zr_{0.5}Ce_{0.5}O_2$–AluCev[b]	29	3.8	17	6.4
$Zr_{0.5}Ce_{0.5}O_2$–AluCsp[b]	35	3.1	24	4.6
CeO_2–Puralox[b]	41	2.7	28	3.9
CeO_2–AluCev[b]	26	4.2	10	10.6
CeO_2–AluCsp[b]	37	3.0	21	5.0
$20Zr_{0.5}Ce_{0.5}O_2$–Puralox[b]			29	3.8
$20Zr_{0.25}Ce_{0.75}O_2$–Puralox[b]			32	3.4
$Zr_{0.25}Ce_{0.75}O_2$–Puralox[b]	38	2.9	31	3.6

[a] Measurements performed at 303 K.
[b] Measurements performed at 195 K.

that Puralox calcined at 1173 K presents a S_{BET} higher than AluC (82 m^2/g $S_{BET,AluC}$, 162 m^2/g $S_{BET,Puralox}$). However, when the calcination temperature is over 1373 K a significant drop on the Puralox sample (less than 20 m^2/g) is found, whereas $S_{BET,AluC}$ remains with a stable value around 80 m^2/g. Additionally AluC presents high surface areas (60 m^2/g) even for calcinations at 1423 K for 5 h. The results for the aged alumina powders after the water treatment are presented in the same figures. It is observed that the water treatment has a detrimental effect on the surface area in both materials, being more pronounced in the AluC case. For example, when the samples are calcined at 1273 K, all the samples have a similar surface are (85 m^2/g S_{BET}). However, when the calcination temperature is raised to 1373 K, lower BET surface area is found on the Puralox and the water treated powders than untreated AluC. By combination of these results with the ones reported previously in the XRD and DTA part, it is noticed that the remarkable decrease of the surface area of the Al_2O_3 is clearly related to the formation of α-Al_2O_3.

In addition the evolution of the BET surface area for CeO_2–Al_2O_3 nanocomposites as a function of the calcination temperature is presented in Fig. 5a and b, for Puralox and AluC-based nanocomposites, respectively. For AluC based samples, both the spray drying and the evaporation-drying method are shown. It is observed that for calcination temperatures below 1300 K the CeO_2–Puralox presents a higher S_{BET} than the CeO_2–AluCev or CeO_2–AluCsp. For example, at 1173 K $S_{BET,\ CeO_2\text{-AluCev}}$ of 80 m^2/g and $S_{BET,\ CeO_2\text{-AluCsp}}$ of 87 m^2/g whereas $S_{BET,\ CeO_2\text{-Puralox}}$ of 105 m^2/g. However, when the calcination temperature is raised to values over 1300 K the CeO_2–AluCev or CeO_2–AluCsp maintain a higher surface area than CeO_2–Puralox, i.e. for an calcination temperature of 1423 K $S_{BET,\ CeO_2\text{-AluCev}}$ of 32 m^2/g and $S_{BET,\ CeO_2\text{-AluCsp}}$ of 68 m^2/g whereas $S_{BET,\ CeO_2\text{-Puralox}}$ of 5 m^2/g. From this comparison, it is observed a detrimental behavior for the CeO_2–AluCev sample when compared with the AluC powder. In addition, a faster decrease of the surface area is found for the Puralox sample than for the CeO_2–Puralox. Puralox is more sensitive to the calcination temperature than AluC or the CeO_2–Al_2O_3 nanocomposites. BET surface area measurements have been also done for the $Zr_{0.5}Ce_{0.5}O_2$–Al_2O_3 nanocomposites. The observed behavior for these group of samples is similar than for the CeO_2–Al_2O_3. For the sake of simplicity, those experimental results are not presented.

The pore structure strongly depends on the synthesis conditions of the material. The aluminas employed in this study present different pore structures as displayed in Fig. 5c and d for materials calcined at 1173 K during 5 h. Whereas Puralox presents a unimodal pore size distribution with a maximum at around 10 nm, AluC presents no porosity. The pore size distribution is strongly affected by the water treatment as shown in Fig. 5c and d. After the water treatment a completely changed distribution is observed for the AluC powder. Thus a Gaussianan-like unimodal distribution is found with a maximum peak around 23 nm. The pore volume is decreasing for the Puralox water treated material and a small shoulder appears around 6 nm. These results agree with those from XRD or DTA where a completely modified behavior is observed for the AluC water treated material. Even though the water treatment did not significantly influence the surface area of alumina powders in the Puralox case, some differences have been found such as a slightly larger contribution of the α-phase at the lower calcination temperature, or an earlier alumina phase transition according to DTA results suggesting a different behavior for the water treated material. In addition, the BET surface area for the samples calcined at 1173 K showed a large drop for the Puralox water treated (130 m^2/g) when compared with the Puralox sample (162 m^2/g) which may explain the larger pore volume of the Puralox material.

The pore size distribution for the CeO_2–alumina nanocomposites is also plotted in the same Fig. 5c and d. It is observed that the introduction of CeO_2 provokes a strong modification on the pore size distribution for all the materials. However, the changes are more obvious for the AluC samples (Fig. 5d). A Gaussian-like unimodal distribution is observed for all the nanocomposites but CeO_2–Puralox shows a narrower distribution and smaller medium pore size where the pore volume diminished due to the introduction of the CeO_2. The observed behavior is similar to the water

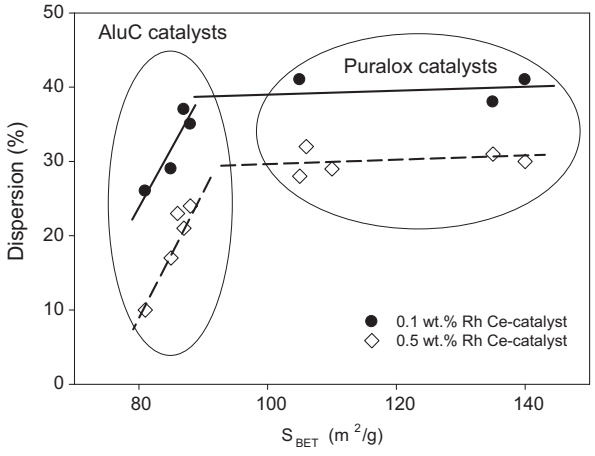

Fig. 6. Variation of the dispersion with the BET surface area for Ce-containing catalysts. Catalysts have been calcined at 1173 K for 5 h. Rh dispersions have been calculated employing H_2-chemisorption at 195 K.

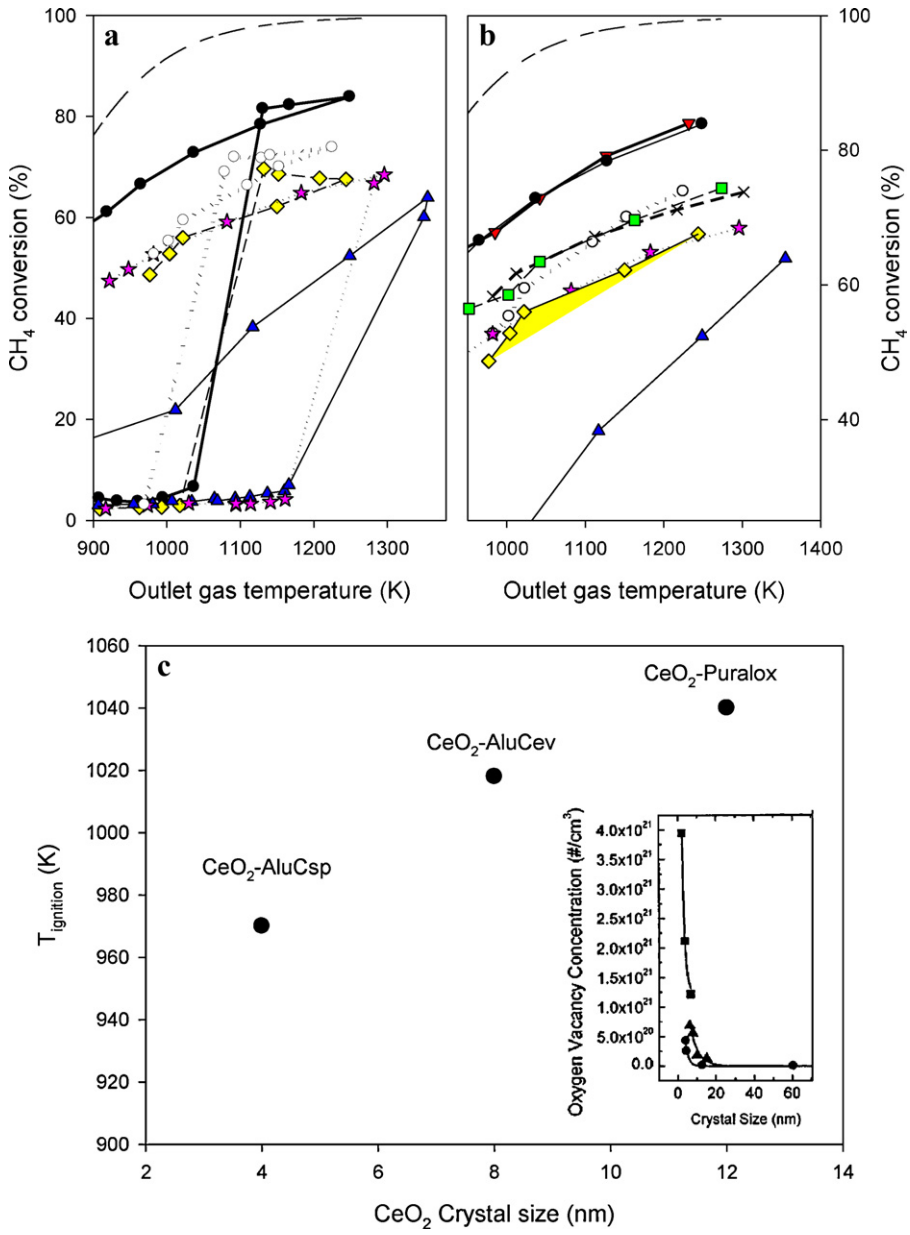

Fig. 7. Comparison of the methane conversions for (a) ignition–extinction behavior $Rh/CeO_2–Al_2O_3$ catalysts and (b) methane conversion for $Rh/Zr_xCe_{1-x}O_2–Al_2O_3$ catalysts after ignition. A Rh loading of 0.1% has been employed. Results are compared with Rh/Al_2O_3 (, Rh/CeO_2–AluCev; ●, Rh/CeO_2–Puralox; ○, Rh/CeO_2–AluCsp; ★, Rh/AluC; ▲, Rh/Puralox; ■, $Rh/Zr_{0.5}Ce_{0.5}O_2$–AluCev; ▼, $Rh/Zr_{0.5}Ce_{0.5}O_2$–Puralox; ×, $Rh/Zr_{0.5}Ce_{0.5}O_2$–AluCsp; —, equilibrium) (P = 1 atm. GHSV = 1500 L_{CH_4}/h g_{cat}, CH_4/O_2 = 2. Outlet gas temperature interval = 573–1300 K. Furnace temperature interval = 573–1173 K). (c) Relation between the ignition temperature and the c-CeO_2 crystal size for 0.1 wt.% $Rh/CeO_2–Al_2O_3$ catalysts. Crystal size calculated in bases of XRD patterns for supports calcined at 1173–1273 K during 5 h. As an inserted in the right corner is presented the variation of the oxygen vacancy concentration with the c-CeO_2 crystal size reported from Zhou and Huebner [64].

treated material but with a slightly lower maximum pore volume value probably due to the slightly lower BET surface area of the nanocomposite calcined at 1173 K. The completely different shape of the curves for the AluC materials indicates a complete rearrangement in the nanocomposites and a strong interaction between ceria and alumina.

Fig. 5e presents the pore size distribution for the powders after calcination at 1423 K for 5 h. The annihilation of the porosity in the alumina samples (Puralox, Puralox water treated and AluC water treated) is ascribed to the formation of the α-alumina. The emergence of peaks at higher pore width and a small shift towards higher mean pore diameter is observed for the CeO_2–Puralox and CeO_2–AluCev nanocomposites, whereas CeO_2–AluCsp remains almost constant. Additionally the mean pore volume is diminished when compared with the samples calcined at 1173 K, probably due to the formation of the α-phase which causes the decrease of the BET surface area and porosity for those nanocomposites.

3.3. Hydrogen chemisorption

Different Rh loadings, namely, 0.1 and 0.5 wt.% are used here. Prior to the chemisorption, the Rh supported on the composite samples are calcined at 1173 K for 5 h. The dispersions of the Rh over these different supports, measured at 303 and 191 K after reduction at 923 K for 1 h, are showed in Table 1.

The presence of H_2 spillover is a significant concern when measuring the H_2-chemisorption in cerium containing catalyst due to an extensive adsorption of H_2 on the CeO_2 itself [33,61]. It has been reported [57,62] that an independent criterion for discriminating the presence of spillover is the time to reach the equilibrium. For all

the catalysts measured here, the H_2 adsorption on the metal was equilibrated within approx. 28 min at an equilibrium pressure of 2 mmHg which are observed independently of the cerium content of the support, suggesting the absence of spillover.

Catalysts prepared with the Puralox powders present a higher dispersion than those prepared with the AluC ones regardless the method employed in the former case. Additionally, slightly higher values are measured in the case of the AluCsp when compared with AluCev. This aspect is supported for both groups of samples but remarkably observed for the CeO_2–Al_2O_3 nanocomposites. Thus, for the 0.5 wt.% Rh loading double Rh particle size is calculated from the H_2-chemisorption results for the catalyst prepared by evaporation when compared with the one by spray drying.

Fig. 6 correlates the BET surface area of the Ce-containing catalyst supports with the dispersions of Rh calcined at 1173 K for 5 h. The corresponding dispersion and particle size of Rh over these supports are also shown in Table 1. According to our results, the Rh dispersion is strongly dependent on the surface area for the AluC catalysts. Thus, when the supports are prepared by evaporation-drying a lower surface area is achieved compared to the spray drying procedure. This lower surface area leads to a poorer Rh dispersion. However, when the surface area is large enough, the dispersion becomes independent of the S_{BET}. Then, just a small variation on the dispersion values is found for the Puralox catalysts containing CeO_2 in the S_{BET} interval from 110 to 150 m^2/g.

3.4. Catalytic performance of Rh-supported catalysts over partial oxidation of methane

3.4.1. Ignition–extinction behavior and methane conversion for catalysts with a loading of 0.1 wt.%

A study on Puralox based catalysts with a loading of Rh 0.5 wt.% and 0.1 wt.% has been previously reported [59]. The activity of 0.5 wt.% Rh catalysts is very high and the conversions were close to the equilibrium at the conditions studied, regardless of the support.

Fig. 7a and b displays a comparison of the methane conversion for catalysts supported in AluC and Puralox nanocomposites with a Rh loading of 0.1 wt.%. Fig. 7a presents the catalytic performance regarding the Rh/CeO_2–Al_2O_3 catalysts compared with Rh/Al_2O_3, whereas Fig. 7b gives a comparison of the catalytic performance after ignition for Rh/$Zr_xCe_{1-x}O_2$–Al_2O_3 catalysts. Better catalytic performance is achieved for nanocomposites supported on $Zr_xCe_{1-x}O_2$–Al_2O_3 than for the Rh/Al_2O_3 catalysts, showing lower light off temperatures and higher conversions. This behavior is in agreement with our previous results where we have shown that the presence of Ce enhances the catalytic performance and provides lower ignition temperatures for CPO [59].

The relationship between the c-CeO_2 crystal size in the CeO_2–Al_2O_3 nanocomposites and the ignition temperature is presented in Fig. 7c. The c-CeO_2 crystal size values have been calculated with Topas software. The values for nanocomposites calcined at 1273 K for 5 h are reported in the figure. Those samples are selected due to the difficulties for the calculation of the crystal size for the materials after calcination at 1173 K because of the small c-CeO_2 crystal size. Thus, lower crystal sizes are expected for the nanocomposites calcined at 1173 K for 5 h. It is observed that the lower c-CeO_2 crystal size implies the lower ignition temperature for methane partial oxidation. It has been previously reported [63–65] that by decreasing the particle size the lattice parameter increases due to the loss of O_2 from the surface region of CeO_2 particles. Additionally, it has been confirmed the existence of Ce^{3+} ions in small particles and the increased ratio of Ce^{3+}/Ce^{4+} at the surface with decreasing size [63,65]. Thus, the lattice expansion was due to the presence of a larger concentration of oxygen vacancies, as showed as an inserted in Fig. 7c [64]. The formation of oxygen vacancies will result in an enhanced reducibility, thus lower ignition temperature, as presented in Fig. 7c for Rh/CeO_2–Al_2O_3 catalysts. Besides, as observed in the inserted figure, the increase of oxygen vacancies with the smaller c-CeO_2 crystal size is strongly enhanced for sizes in the range between 1 and 10 nm. Thus, ceria crystal size larger than 20 nm would not provide any difference regarding the oxygen vacancy concentration. Moreover, it is known that on ceria the oxygen storage capacity is restricted to the surface, because the bulk oxygen atoms do not participate in the storage process [66,67]. Consequently, it is confirmed the great importance of providing a highly dispersed layer of CeO_2 on the alumina surface.

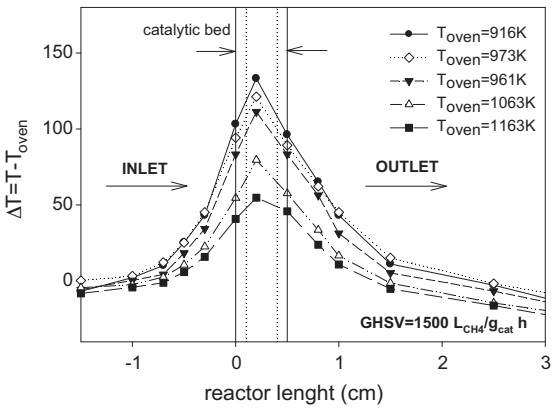

Fig. 8. Typical axial temperature profile as function of the oven temperature between 916 and 1163 K (catalyst: 0.5 Rh/$Zr_{0.5}Ce_{0.5}O_2$–AluCev, GHSV = 1500 $L_{CH_4}/h\ g_{cat}$). Vertical solid lines are showing the beginning and end of the catalytic bed. Vertical dotted lines show the end and beginning of the α-alumina inert layers.

After ignition, catalysts containing Puralox show higher methane conversions compared with the AluC catalysts as presented in Fig. 7b. At an outlet gas temperature of 1150 K, the activity follows an order of Rh/$Zr_{0.5}Ce_{0.5}O_2$–Puralox = Rh/CeO_2–Puralox (81% conversion) > Rh/$Zr_{0.5}Ce_{0.5}O_2$–AluCsp = Rh/$Zr_{0.5}Ce_{0.5}O_2$–AluCev = Rh/CeO_2–AluCsp (75% conversion) > Rh/CeO_2–AluCev = Rh/AluC (67% conversion) > Rh/Puralox. Rh/CeO_2–AluC catalyst prepared with the spray dryer presents higher methane conversion than the one prepared by evaporation. However, in the case of Rh/$Zr_{0.5}Ce_{0.5}O_2$–AluC catalysts, a similar catalytic performance is achieved after ignition regardless of the use of the support prepared with the spray dryer or the evaporation method. The catalytic performance is clearly following the same trend as the Rh dispersions shown in Table 1. This is particularly obvious for the case of the Rh/CeO_2–Al_2O_3 catalysts where the catalyst supported on CeO_2–Puralox is having a Rh dispersion of 41%, followed by CeO_2–AluCsp with 37% and CeO_2–AluCev with 26%.

3.4.2. Stability

Fig. 8 shows temperature profiles in the catalytic bed for increased oven temperatures for a 0.5 wt.% Rh/$Zr_{0.5}Ce_{0.5}O_2$–AluCev catalyst. The temperature profiles indicate that the reaction proceeds through the indirect mechanism, consisting of a total oxidation of some methane followed by the endothermic steam reforming and probably water–gas shift reaction. The increase in the oven temperature provokes a decrease in the exothermic peak intensity. At higher temperatures the steam reforming rate is higher, thus it enables to offset the heat released by the combustion.

Stability is a key factor in methane partial oxidation due to the very high temperature reached during the reaction. It is under those conditions where the catalytic performance of the materials is here studied. An oven temperature of 1173 K is selected with the objective of comparing the thermal stability of the studied catalysts.

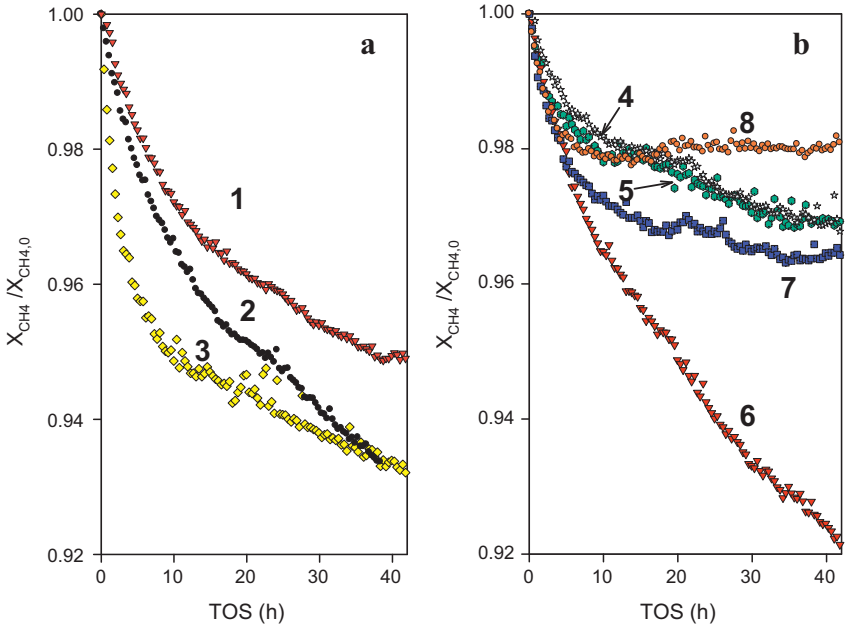

Fig. 9. Comparison ratio between the CH_4 conversion and the initial CH_4 conversion during 42 h reaction for (a) Puralox catalysts (▼ $Rh/Zr_{0.5}Ce_{0.5}O_2$–Puralox (1); ●, Rh/CeO_2–Puralox (2); , Rh/Puralox (3)) and (b) AluC catalysts (☆ , Rh/AluC (4); ⬢ , $Rh/Zr_{0.5}Ce_{0.5}O_2$–AluCev (5); ▼ Rh/CeO_2–AluCev (6); , Rh/CeO_2–AluCsp (7); ●, $Rh/Zr_{0.5}Ce_{0.5}O_2$–AluCsp (8)) (Rh loading = 0.5 wt.%, P = 1 atm, GHSV = 1500 L_{CH_4}/h g_{cat}, T_{max} = 1230 K, $T_{furnace}$ = 1173 K, CH_4/O_2 = 2).

Fig. 9a and b presents a comparison of the deactivation rate for the Puralox and AluC based catalysts respectively. The deactivation rate is calculated as the ratio between the conversion at time "t" and the initial conversion. Catalysts with a Rh loading of 0.5 wt.% are tested during 48 h. It is noticed that almost complete oxygen conversion is achieved at the outlet of the reactor.

It is realized that all the catalysts supported on the nanocomposites ($Zr_xCe_{1-x}O_2$–Al_2O_3) present a higher conversion than the unmodified alumina catalysts (Rh/Puralox and Rh/AluC). In the initial period of the experiments those catalyst based on Puralox powders present the highest conversion due to the higher Rh dispersion, as reported in Table 1. Interestingly, it is observed that the AluC catalyst prepared by spray drying method presents a much better stability than those prepared by evaporation. Puralox-based catalysts present a continuous deactivation during the 48 h. Among them, the most stable performance is achieved for the catalyst supported on $Zr_{0.5}Ce_{0.5}O_2$–Puralox. Previously we have reported that the formation of the cerium aluminate might give an explanation of this behavior [59]. Additionally, the same trend is observed in the three groups of samples, with a lower deactivation rate for catalysts supported on $Zr_{0.5}Ce_{0.5}O_2$––alumina than CeO_2–alumina confirming these results. Moreover, the more pronounced deactivation rate is found for Rh/CeO_2–AluCev in Fig. 9b. The formation of α-Al_2O_3, as shown in Fig. 1b, might be given as a possible reason for this behavior. CeO_2–AluCev supports showed the formation of α-Al_2O_3 after calcination at 1373 K during 24 h. 85% of the alumina presented in such material was under the α-phase, whereas none was observed for the AluCsp sample, and a small fraction for the Puralox one. Nevertheless, the formation of α-Al_2O_3 is drastically delayed when the spray drying is employed as shown in Fig. 1a. Such a feature could give a reason for the better stability observed for the Rh/CeO_2–AluCsp catalyst. Additionally, the evolution of the BET surface area with the calcination temperature presented in Fig. 5a and b is also helpful for understanding better the observed deactivation behavior. Thus, the higher deactivation rate of the catalysts supported on Puralox nanocomposites (Fig. 9a) would be quite likely related with a strong decrease of the BET surface area of the support which would lead to the sintering of the Rh particles. However, the AluC supports present a smaller variation on the BET surface area values for the increased calcination temperatures (Fig. 5b), leading to a more stable catalytic behavior. This is clearly confirmed by the catalyst supported in CeO_2–AluCsp (7) when compared with the ones supported on CeO_2–AluCev (6) or CeO_2–Puralox (2) in Fig. 9a and b.

4. Conclusions

Alumina based nanocomposites have been synthesized through a citrate mediated route by modifying the alumina with cerium and zirconium nitrates. The effect of the alumina type has been studied by employing two different raw materials. The slow evaporation-drying route has a remarkable negative effect in the properties of the alumina called AluC. It is notice that the nanocomposites prepared through the evaporation-drying procedure show worse properties for AluC than for Puralox, as indicated by the fact that α-alumina is detected at lower temperatures in AluCev nanocomposites than in Puralox nanocomposites.

Two methods have been employed for the synthesis of AluC based catalysts. The spray drying method has shown to be promising for the preparation of a stable support where the formation of α-alumina is delayed until calcination at 1473 K, providing a suitable media for stabilizing the Rh nanoparticles.

A higher resistance towards sintering and a delayed alumina phase transition is observed for the $Zr_{0.5}Ce_{0.5}O_2$–Al_2O_3 supports when compared with the CeO_2–Al_2O_3 ones. The introduction of zirconia into the ceria lattice leads to a better thermal stability by limiting the growth of the ceria crystals. Therefore higher surface areas and Rh dispersions are achieved leading to a better catalytic performance when Rh is supported on $Zr_{0.5}Ce_{0.5}O_2$–Al_2O_3.

The supports are impregnated with Rh and tested in CPO after calcination at 1173 K for 5 h. Slightly higher dispersions are found with those catalysts synthesized employing Puralox, probably due to their high BET surface area. Additionally AluCsp supports present slightly higher surface area than AluCev leading to lower Rh particle sizes after impregnation and calcination. Thus, Puralox catalysts would lead to the higher conversion under testing conditions. The light off temperature for methane partial oxidation is found to be related with the c-CeO_2 crystal size in the nanocomposites. Lower

c-CeO_2 crystal sizes would lead to lower ignition temperatures, probably due to the higher oxygen vacancy concentration.

Regarding the stability, it is found that Rh/CeO_2–AluCev and Rh/CeO_2–Puralox present a gradual deactivation. Highly active and stable catalytic performance has been achieved on Rh/$Zr_{0.5}Ce_{0.5}O_2$–AluC prepared by spray drying. The observed behavior might be related with the better thermal stability of the support. Concluding, a better catalytic performance to CPO can be achieved by designing properly a support material where Rh particles would be highly dispersed and stabilized.

Acknowledgements

Estelle Vanhaecke is acknowledged for performing the Raman measurements. The financial support from the Norwegian Research Council and Statoil is greatly acknowledged.

References

[1] B.C. Enger, R. Lødeng, A. Holmen, Applied Catalysis A: General 346 (2008) 1.
[2] L. Pino, V. Recupero, S. Beninati, A.K. Shukla, M.S. Hegde, P. Bera, Applied Catalysis A: General 225 (2002) 63.
[3] C. Elmasides, T. Ioannides, X. Verykios, Studies in Surface Science and Catalysis 119 (1998) 801.
[4] M. Prettre, C. Eichner, M. Perrin, Transactions of Faraday Society (1946) 335b.
[5] B.C. Enger, R. Lødeng, A. Holmen, Journal of Catalysis 262 (2009) 188.
[6] R. Lanza, S.G. Järås, P. Canu, Applied Catalysis A: General 325 (2007) 57.
[7] M. Fathi, F. Monnet, Y. Schuurman, A. Holmen, C. Mirodatos, Journal of Catalysis 190 (2000) 439.
[8] L. Basini, A. Aragno, G. Vlaic, Catalysis Letters 39 (1996) 49.
[9] K. Heitnes Hofstad, J.H.B.J. Hoebink, A. Holmen, G.B. Marin, Catalysis Today 40 (1998) 157.
[10] J.J. Spivey, Catalysis, The Royal Society of Chemistry, 2000.
[11] R. Horn, K.A. Williams, N.J. Degenstein, A. Bitsch-Larsen, D. Dalle Nogare, S.A. Tupy, L.D. Schmidt, Journal of Catalysis 249 (2007) 380.
[12] D. Dissanayake, M.P. Rosynek, K.C.C. Kharas, J.H. Lunsford, Journal of Catalysis 132 (1991) 117.
[13] C. Elmasides, T. Ioannides, X.E. Verykios, D.S.F.F.A.V.A. Parmaliana, A.F., Studies in Surface Science and Catalysis, vol. 119. 1998, Elsevier, p. 801.
[14] J.-D. Grunwaldt, S. Hannemann, C.G. Schroer, A. Baiker, The Journal of Physical Chemistry B 110 (2006) 8674.
[15] A. Beretta, G. Groppi, M. Lualdi, I. Tavazzi, P. Forzatti, Industrial & Engineering Chemistry Research 48 (2009) 3825.
[16] M. Maestri, D. Vlachos, A. Beretta, P. Forzatti, G. Groppi, E. Tronconi, Topics in Catalysis 52 (2009) 1983.
[17] M. Maestri, D.G. Vlachos, A. Beretta, G. Groppi, E. Tronconi, AIChE Journal 55 (2009) 993.
[18] S. Hannemann, J.-D. Grunwaldt, B. Kimmerle, A. Baiker, P. Boye, C. Schroer, Topics in Catalysis 52 (2009) 1360.
[19] M. Bizzi, L. Basini, G. Saracco, V. Specchia, Chemical Engineering Journal 90 (2002) 97.
[20] J. Wei, E. Iglesia, Journal of Catalysis 225 (2004) 116.
[21] A.K. Neyestanaki, F. Klingstedt, T. Salmi, D.Y. Murzin, Fuel 83 (2004) 395.
[22] M. Ozawa, M. Kimura, A. Isogai, Journal of the Less Common Metals 162 (1990) 297.
[23] X. Wu, B. Yang, D. Weng, Journal of Alloys and Compounds 376 (2004) 241.
[24] Y. Jia, Y. Hotta, K. Sato, K. Watari, Journal of the American Ceramic Society 89 (2006) 1103.
[25] R. Di Monte, P. Fornasiero, J. Kaspar, M. Graziani, J.M. Gatica, S. Bernal, A. Gómez-Herrero, Chemical Communications (2000) 2167.
[26] B. Reddy, A. Khan, Catalysis Surveys from Asia 9 (2005) 155.
[27] P.P. Silva, F.A. Silva, H.P. Souza, A.G. Lobo, L.V. Mattos, F.B. Noronha, C.E. Hori, Catalysis Today 101 (2005) 31.
[28] J. Wang, J. Wen, M. Shen, The Journal of Physical Chemistry C 112 (2008) 5113.
[29] S. Rossignol, C. Kappenstein, International Journal of Inorganic Materials 3 (2001) 51.
[30] A. Vazquez, T. Lopez, R. Gomez, X. Bokhimi, Journal of Molecular Catalysis A: Chemical 167 (2001) 91.
[31] A. Talo, J. Lahtinen, P. Hautojärvi, Applied Catalysis B: Environmental 5 (1995) 221.
[32] M.H. Yao, R.J. Baird, F.W. Kunz, T.E. Hoost, Journal of Catalysis 166 (1997) 67.
[33] R. Di Monte, P. Fornasiero, J. Kaspar, P. Rumori, G. Gubitosa, M. Graziani, Applied Catalysis B: Environmental 24 (2000) 157.
[34] R. Di Monte, P. Fornasiero, S. Desinan, J. Kaspar, J.M. Gatica, J.J. Calvino, E. Fonda, Chemistry of Materials 16 (2004) 4273.
[35] P.P. Silva, F. de, A. Silva, A.G. Lobo, H.P. de Souza, F.B. Passos, C.E. Hori, L.V. Mattos, F.B. Noronha, B. Xinhe, X. Yide, Studies in Surface Science and Catalysis, vol. 147, Elsevier, 2004, p. 157.
[36] P.P. Silva, F.A. Silva, L.S. Portela, L.V. Mattos, F.B. Noronha, C.E. Hori, Catalysis Today 107–108 (2005) 734.
[37] F.B. Noronha, E.C. Fendley, R.R. Soares, W.E. Alvarez, D.E. Resasco, Chemical Engineering Journal 82 (2001) 21.
[38] L. De Rogatis, T. Montini, M.F. Casula, P. Fornasiero, Journal of Alloys and Compounds 451 (2008) 516.
[39] T. Montini, L. De Rogatis, V. Gombac, P. Fornasiero, M. Graziani, Applied Catalysis B: Environmental 71 (2007) 125.
[40] M.M.V.M. Souza, M. Schmal, Applied Catalysis A: General 281 (2005) 19.
[41] J.C. Escritori, S.C. Dantas, R.R. Soares, C.E. Hori, Catalysis Communications 10 (2009) 1090.
[42] L.S.F. Feio, C.E. Hori, S. Damyanova, F.B. Noronha, W.H. Cassinelli, C.M.P. Marques, J.M.C. Bueno, Applied Catalysis A: General 316 (2007) 107.
[43] M. Fernández-García, A. Martínez-Arias, A. Iglesias-Juez, A.B. Hungría, J.A. Anderson, J.C. Conesa, J. Soria, Applied Catalysis B: Environmental 31 (2001) 39.
[44] B. Reddy, P. Saikia, P. Bharali, Catalysis Surveys from Asia 12 (2008) 214.
[45] S. Letichevsky, C.A. Tellez, R.R.d. Avillez, M.I.P.d. Silva, M.A. Fraga, L.G. Appel, Applied Catalysis B: Environmental 58 (2005) 203.
[46] A.I. Kozlov, D.H. Kim, A. Yezerets, P. Andersen, H.H. Kung, M.C. Kung, Journal of Catalysis 209 (2002) 417.
[47] Q. Zhang, J. Wen, M. Shen, J. Wang, Journal of Rare Earths 26 (2008) 700.
[48] Z. Wei, H. Li, X. Zhang, S. Yan, Z. Lv, Y. Chen, M. Gong, Journal of Alloys and Compounds 455 (2008) 322.
[49] V.B. Mortola, J.A.C. Ruiz, L.V. Mattos, F.B. Noronha, C.E. Hori, Catalysis Today 133–135 (2008) 906.
[50] A. Morikawa, T. Suzuki, T. Kanazawa, K. Kikuta, A. Suda, H. Shinjo, Applied Catalysis B: Environmental 78 (2008) 210.
[51] A. Martinez-Arias, M. Fernandez-Garcia, L.N. Salamanca, R.X. Valenzuela, J.C. Conesa, J. Soria, The Journal of Physical Chemistry B 104 (2000) 4038.
[52] J. Regalbuto, Catalyst Preparation: Science and Engineering, CRC Press Taylor & Francis Group, Boca Raton, 2006.
[53] T. Zhao, S. Boullosa-Eiras, Y. Yu, D. Chen, A. Holmen, M. Rønning, Topics in Catalysis, submitted for publication.
[54] H.M. Rietveld, Journal of Applied Crystallography 2 (1969) 65.
[55] G.S. Pawley, Journal of Applied Crystallography 14 (1981) 357.
[56] J.M. Gatica, R.T. Baker, P. Fornasiero, S. Bernal, G. Blanco, J. Kaspar, The Journal of Physical Chemistry B 104 (2000) 4667.
[57] J.M. Gatica, R.T. Baker, P. Fornasiero, S. Bernal, J. Kaspar, The Journal of Physical Chemistry B 105 (2001) 1191.
[58] S. Boullosa-Eiras, E. Vanhaecke, T. Zhao, D. Chen, A. Holmen, Catalysis Today, in press.
[59] S. Boullosa-Eiras, T. Zhao, E. Vanhaecke, D. Chen, A. Holmen, submitted to Catalysis today.
[60] A.E. McHale, Phase diagrams for ceramists, Annual 1991, 1991.
[61] A. Trovarelli, Catalysis by Ceria and Related Materials, World Scientific Publishing Company, London, 2002.
[62] P. Fornasiero, J. Kaspar, T. Montini, M. Graziani, V. Dal Santo, R. Psaro, S. Recchia, Journal of Molecular Catalysis A: Chemical 204–205 (2003) 683.
[63] L. Wu, H.J. Wiesmann, A.R. Moodenbaugh, R.F. Klie, Y. Zhu, D.O. Welch, M. Suenaga, Physical Review B 69 (2004) 125415.
[64] X.-D. Zhou, W. Huebner, Applied Physics Letters 79 (2001) 3512.
[65] S. Tsunekawa, K. Ishikawa, Z.Q. Li, Y. Kawazoe, A. Kasuya, Physical Review Letters 85 (2000) 3440.
[66] S. Bedrane, C. Descorme, D. Duprez, Catalysis Today 75 (2002) 401.
[67] Y. Madier, C. Descorme, A.M. Le Govic, D. Duprez, The Journal of Physical Chemistry B 103 (1999) 10999.